Porous airfoils: noise reduction and boundary layer effects

Thomas Geyer, Ennes Sarradj and Christoph Fritzsche
Aeroacoustics Group, Brandenburg University of Technology, 03046 Cottbus, Germany

The present paper describes acoustic and hot–wire measurements that were done in the aeroacoustic wind tunnel at the Brandenburg University of Technology Cottbus on various SD7003–type airfoils made of different porous (flow permeable) materials. The objective of the research is the analysis of the turbulent boundary layer properties of porous airfoils and, subsequently, of the noise generated at the trailing edge. The influence of the porous materials, characterized by their air flow resistivity, is discussed. The acoustic measurements were performed using a planar 56–channel microphone array and the boundary layer properties were measured using constant temperature anemometry. The recorded acoustic data underwent further processing by application of advanced beamforming algorithms. A noticeable reduction of the emitted trailing edge noise was measured for the porous airfoils over a large range of frequencies. At high frequencies, some of the porous airfoils were found to generate more noise than the reference airfoil which might be due to the surface roughness noise contribution. It is found that the turbulent boundary layer thickness and the boundary layer displacement thickness of the airfoils increase with decreasing flow resistivities for both suction and pressure side. Both boundary layer thickness and displacement thickness of the porous airfoils are greater than those of a non-porous reference airfoil

NOMENCLATURE

c	speed of sound, m/s
c_l	chord length, m
d	wind tunnel nozzle diameter, m
D	directivity function
f	frequency, Hz
h	span width wetted by the flow, m
Ma	mean flow Mach number
n	scaling exponent
$OASPL$	overall sound pressure level, dB
$\langle p^2 \rangle$	far field mean square sound pressure, Pa^2
r	air flow resistivity, Pa s/m^2
R	distance, m
Re	chord based Reynolds number
SPL	(third octave band) sound pressure level, dB
Sr	chord based Strouhal number
Tu	turbulence intensity, %
u'	turbulent velocity fluctuations, m/s
$\overline{u}$	mean flow velocity, m/s
U	mean flow speed outside the boundary layer, m/s
x, y, z	cartesian coordinates, m
α	(geometric) angle of attack, °
δ	(99%) boundary layer thickness, m
δ_1	boundary layer displacement thickness, m
δ_2	boundary layer momentum thickness, m
δ_3	boundary layer energy thickness, m
Δp	pressure difference, Pa
Δx	sample thickness, m
ℓ	characteristic turbulence correlation scale, m
ρ	medium density, kg/m^3

1. INTRODUCTION

Against the background of rising needs for quiet aircraft, turbine blades and fans, different methods and approaches for airfoil self noise control are used and constantly improved in the field of aeroacoustics. One possible solution is the use of porous, flow–permeable materials. Porous or partly porous airfoils as a means of noise reduction

have been subject to several studies before. This includes research on the aeroacoustic and the aerodynamic effects of porous airfoils in a fluid flow. Chanaud et al. [1, 2] describe the effect of porous blades on the reduction of fan noise. Savu [3] did numerical analysis on the use of porous materials to affect the pressure jump on airfoils in transsonic flow. Mineck and Hartwich [4] did extensive aerodynamic experiments with partly porous airfoils in an open jet wind tunnel. The publications by Tinetti et al. [5, 6] contain the use of a passive porosity to reduce wake–stator–interaction noise. Garcia-Sagrado et al. [7] invested the trailing edge noise generation on model airfoils with different trailing edge thicknesses by measuring both surface pressure fluctuations and turbulent boundary layer velocity. Geyer et al. [8] and Sarradj and Geyer [9] conducted aeroacoustic measurements on a large set of porous airfoils. Herr [10] did research on the influence of a flow–permeable trailing edge on the noise generation. Her results also confirmed the noise reduction potential of flow permeable trailing edges. The results described in reference [8] encourage further measurements to help understand the influence of the porous material parameters on the boundary layer properties and the sound reduction of the porous airfoils.

The aim of the present paper is the investigation of the development of the turbulent boundary layer at porous airfoils, which are characterized by their air flow resistivity, and on the subsequent generation of airfoil self noise. To this purpose, different airfoil models made completely out of porous materials were subjected to a virtually non–turbulent air flow. Aeroacoustic and hot–wire measurements were then carried out in order to gain knowledge on the boundary layer properties, especially the displacement thickness, and their correlation to the airfoil self noise emission. The focus of the present research is on the turbulent boundary layer - trailing edge noise only as the most important airfoil noise source for a virtually non–turbulent inflow. According to Blake [11], leading and trailing edges of an airfoil in a fluid flow can be viewed as independent noise sources, if

$$f > \frac{c}{c_l}, \tag{1}$$

f being the frequency, c the speed of sound and c_l the airfoil chord length. In the present research, Equation 1 leads to a lower frequency limit of approximately 1.5 kHz. Above this frequency, the trailing edge noise can therefore be examined separately.

The influence of certain boundary layer properties, especially the boundary layer displacement thickness δ_1, on the sound generation at the trailing edge has been the subject of many scientific studies before, most of which are based on the work of Lighthill [12]. One fundamental study based on Lighthill's findings is the work of Ffowcs Williams and Hall [13]. They gave a formulation for the far field mean square sound pressure $\langle p^2 \rangle$ produced by a turbulent flow over a scattering halfplane:

$$\langle p^2 \rangle \propto \rho^2 \overline{u}^2 \frac{U^3}{c} \left(\frac{h\ell}{R^2} \right) \cdot \bar{D}, \tag{2}$$

with ρ being the medium density, $\overline{u}^2$ the mean–square turbulence velocity, U the mean flow speed outside the boundary layer, h the spanwise extent wetted by the flow, ℓ a characteristic turbulence correlation scale, R the distance of the observer and $\overline{D}$ a directivity factor ($\overline{D} = 1$ for observers normal to the surface of the plate). This analytical edge–scatter formulation describes the sound emission based on boundary layer parameters. As reported by Brooks and

Marcolini [14] the usual assumptions are that the characteristic turbulence correlation scale is proportional to the turbulent boundary layer thickness δ or the turbulent boundary layer displacement thickness ($\ell \propto \delta \propto \delta_1$) and the mean turbulence velocity is proportional to the mean flow speed ($\overline{u} \propto U$). According to Equation 2 the far field sound pressure increases for an increasing characteristic turbulence correlation scale at a constant flow speed, thus for an increasing boundary layer thickness or displacement thickness. Beside this analytical model, Ffowcs Williams and Hall formulated a scaling approach for trailing edge noise that is commonly used in the field of aeroacoustics: The sound pressure level (SPL) of the sound emitted at the trailing edge of a halfplane caused by a turbulent flow over the edge scales with a power of the flow speed U:

$$SPL_{scaled} = SPL - 10 \cdot log_{10}\left(\frac{U}{1\ \mathrm{m/s}}\right)^{n} \mathrm{dB}. \quad (3)$$

Ffowcs Williams and Hall found the exponent to be $n = 5$. Howe [15] stated in his review of different trailing edge noise theories that the turbulent boundary layer - trailing edge noise sound power scales with the 4.6th power of the flow speed, thus leading to $n = 4.6$ in Equation 3. Additionally, Howe formulated a basic theory on the influence of the displacement thickness on the noise generated at a sharp trailing edge [16]. Other studies concerning airfoil self noise include the work of Brooks and Hodgson [17], who determined the influence of the trailing edge geometry, mainly the trailing edge bluntness, on the airfoil self noise. Another fundamental work is the report by Brooks, Pope and Marcolini [18], containing detailed examinations of five main airfoil self noise sources. Their semi–empirical noise prediction model (the BPM–model), that includes a normalization based on the theory of Ffowcs Williams and Hall (see reference [14]), is still used in aeroacoustic studies today. The sound pressure is also scaled using Equation 3, the exponent ranging from approximately 4.6 to 5.0 depending on the Reynolds number. Other studies on the generation of sound at the trailing edge are the research done by Grosveld [19] and by Lowson [20, 21], both resulting in relatively simple noise prediction models for wind turbines, and the experimental work reported by Oerlemans et al. [22, 23]. The latter found the exponent $n = 4.5$ for the scaling of the trailing edge noise using Equation 3. A freely available software for the prediction of airfoil self noise, called NAFNoise [24] (National Renewable Energy Laboratory AirFoil Noise), exists which combines different models, for example the BPM–model mentioned above.

Additional research was done in the past to identify the influence of a certain surface roughness of a wall on the sound generation, for example by Howe [25, 26], Liu et al. [27, 28] and Grissom [29]. Howe described the sound that is generated by a turbulent boundary layer flow over a rough surface, which is modeled as a distribution of rigid, hemispherical bosses on a rigid plane. He found that, in accordance to experimental data by Hersh [30], for a given surface roughness the associated roughness noise decreases for increasing thicknesses of the turbulent boundary layer. According to his studies, roughness noise scales with the 6th power of the flow speed for small Mach numbers. The influence of a surface roughness on the evolution of the boundary layer turbulence was not taken into account.

In 2006 a first study by Liu et al. [27] included an empirical and numerical model for turbulent boundary layer flow over a rough wall.

The numerical model was used to predict the roughness noise from an aircraft wing and the results were compared to the trailing edge noise of a (smooth) wing of the same size and shape. They found that the roughness noise is noticeable at high frequencies, where it can be more significant than the corresponding trailing edge noise. At low frequencies on the other hand, the influence of the roughness noise on the trailing edge noise is negligible. However, the contribution of the roughness noise is proportional to the size and the density of the roughness elements. To validate the models, Liu et al. did microphone array measurements on rough and smooth plates in an open jet wind tunnel, where the noise of the rough plates exceeded that of the smooth plate for frequencies between approximately 1 and 2.5 kHz. In 2007, Liu et al. [28] performed extensive microphone array experiments with one low–frequency and one high–frequency array on rough plates and compared the results to those of smooth plates. They confirmed the results from their 2006 study and found that the roughness noise of the rough plates enhanced the trailing edge noise due to an increased boundary layer thickness.

The effect of a surface roughness is widely used for the tripping of a laminar boundary layer to enforce the generation of a turbulent boundary layer (transition). The effect of tripping devices on the boundary layer transition is described in detail by Braslow and Knox [31] and Barlow et al. [32]. It is, however, very difficult to describe the influence of the surface roughness in only a few parameters, because the character of the roughness of two surfaces can be quite different from each other [33]. For example, Liu et al. [27, 28] characterized the roughness of their model surfaces by a roughness height and a roughness density. In the work presented in this paper, the roughness of the different airfoils has not been measured due to the difficulties of such measurements on existing porous materials with microscopic structures that vary strongly.

Based on detailed results from extensive aeroacoustic measurements on a set of 16 porous airfoils and one non–porous airfoil presented in reference [8], the purpose of the present paper is the examination of the relation between these acoustic results and the properties of the turbulent boundary layer of the airfoils. To this end hot–wire measurements were done in the boundary layer of a set of four porous airfoils and the non–porous reference airfoil. According to common airfoil trailing edge noise theory, the boundary layer parameters, especially the turbulent boundary layer thickness and the displacement thickness, have a major influence on the trailing edge noise and are therefore widely used for scaling approaches. To enable a better understanding of the flow around porous airfoils and the reduction of trailing edge noise, the influence of the porous materials on the turbulent boundary layer properties and the subsequent noise emission at the trailing edge is examined.

The remainder of this paper is organized as follows: First, the setup that was used for the acoustic measurements and for the hot–wire measurements, including the porous and non–porous airfoil models and the aeroacoustic wind tunnel, is described in detail. Second, the data processing of the acoustic data and of the hot–wire data is explained. Finally, the acoustic results as well as the boundary layer results are presented and discussed.

2. MEASUREMENT SETUP

2.1. AIRFOIL MODELS

One non–porous airfoil and 16 porous airfoils were used in the acoustic experiments. All airfoils have a chord length c_l of 235 mm and a span width of

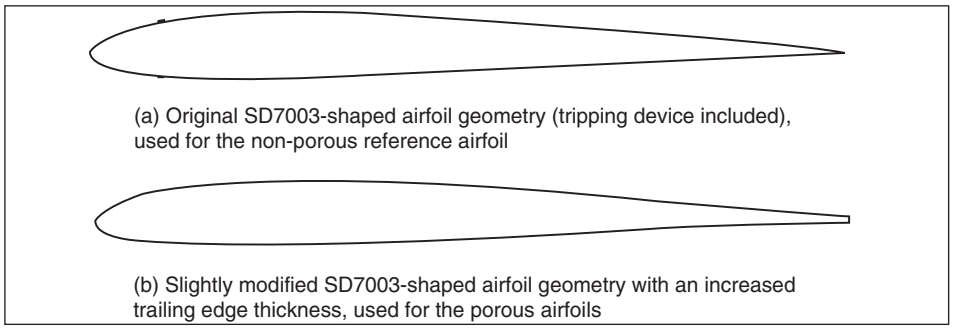

Figure 1. Comparison of the two airfoil designs, both having the same chord length c_l = 235 mm.

approximately 400 mm. The non–porous airfoil serves as a reference to enable comparisons between the different airfoils. It has a SD7003 shape [34], which is a semi–symmetric Low–*Re* airfoil shape, and is tripped at both pressure and suction side at 10.6 % of the chord to ensure the existence of a turbulent boundary layer at the trailing edge (Figure 1(a)). The tripping tape has a chordwise width of 1.6 mm and a height of 0.15 mm. The trailing edge thickness is 0.5 mm. The porous airfoils had a modified SD7003 shape (Figure 1(b)), with a slightly increased trailing edge thickness of 1.59 mm. Without this modification, the trailing edges of the porous airfoils are too fragile to be produced without damage. Due to the surface roughness of the porous materials, no tripping tape needed to be applied to the porous airfoils to trigger the transition to a turbulent boundary layer.

The aim of this research is the analysis of the influence of the porous material parameters on the turbulent boundary layer properties and the sound generation at the trailing edge of the porous airfoils. Most porous materials can be sufficiently characterized by three parameters: porosity, permeability or air flow resistivity and tortuosity. In this paper, the focus is on the air flow resistivity *r* only, because it is assumed to have the biggest impact on both sound and turbulent boundary layer generation.

The air flow resistivity of an open–porous material, where the inner pores are connected to each other and to the ambient fluid, is given by [35]

$$r = \frac{\Delta p}{U \cdot \Delta x}. \qquad (4)$$

Δp is the pressure drop across the porous sample with the thickness Δx and U is the percolation flow speed. That same physical issue is also governed by Darcy's Law, as for example given in reference [36]. The air flow resistivity may take values between 0 (permeable without resistance) and ∞ (impermeable).

A total of 17 airfoil models were originally used for the acoustic measurements (see reference [8]). Only a small subset of those (given in Table 1) were also used for the hot–wire measurements. The reason for this restriction was that a great number of the 16 porous materials is soft, thus preventing the positioning of a hot–wire probe near the porous surface. Therefore, the following sections of this paper concentrate solely on the measurements and results of four rigid porous airfoil models and the non–porous reference airfoil specified in Table 1. A photograph of the porous airfoils can be seen in Figure 2.

The porous airfoils had to be assembled (in the spanwise direction) out of slices (see also Figure 2), because most of the usable porous materials are not available in an appropriate size. The slices were cut out from plates of the porous materials (between

Table 1. Subset of the materials used in the acoustic measurements and in the hot–wire measurements, air flow resistivity r according to Equation 4.

No	Name	Material	Flow resistivity r Pa s/m^2	Color in figures
1	Reference	non–porous	∞	•
2	Porex	sintered PE granulate	316500	•
3	Reapor	sintered glass granulate	16500	•
4	Recemat	metal–foam	8200	•
5	M–Pore Al 45 ppi	metal–foam	1000	•

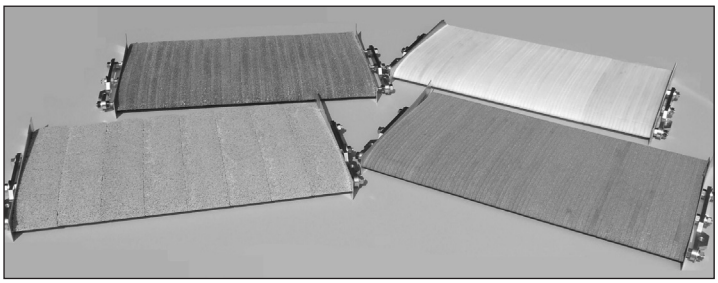

Figure 2. Photograph of the porous airfoils, from upper left to lower right: M–Pore Al 45 ppi, Porex, Reapor, Recemat.

5 mm and 50 mm thick, depending on the material) using water–cut technology. This technique was chosen in order to leave the open–porous surface intact while other techniques, like milling or laser–cutting, would have possibly destroyed or closed the pores due to the high temperatures developing during the process.

2.2. WIND TUNNEL

The acoustic and aerodynamic measurements were conducted in an open jet aeroacoustic wind tunnel. The circular Witoszynski–type nozzle has a diameter d of 0.2 m and a contraction ratio of 16. Note that the span width of the airfoils is greater than the diameter of the nozzle to avoid aeroacoustic and aerodynamic effects at the mountings. The turbulence intensity (in percent) of a flow is calculated using the following equation:

$$Tu = \frac{\sqrt{\overline{u'^2}}}{\overline{u}} \cdot 100\ \%, \qquad (5)$$

with u' being the turbulent velocity fluctuations and $\overline{u}$ being the measured mean flow speed. The measured turbulence intensity in a horizontal line at three different distances to the nozzle exit plane is given in Figure 3(a) for a flow speed of 50 m/s. The measurements were done using a single wire hot-wire probe. Figure 3(a) shows that the turbulence in the core jet is very low. The according flow velocity profiles for the three distances from the nozzle, as specified above, are given in Figure 3(b) for a flow speed of 50 m/s. The A–weighted wind tunnel self noise, measured for different flow speeds in a distance of 1 m at an angle of 90° to the nozzle axis, is shown in Figure 4. It can be seen that the overall sound pressure level (including third octave bands with center frequencies from 100 Hz to 20 kHz) is below 60 dB at a flow speed of 50 m/s.

During the acoustic measurements, the test section in front of the nozzle is surrounded by a cabin with absorbing sidewalls, providing a nearly anechoic acoustic environment for frequencies greater than approximately 500 Hz. Figure 5 shows a photograph of one of the porous airfoils in front of the wind

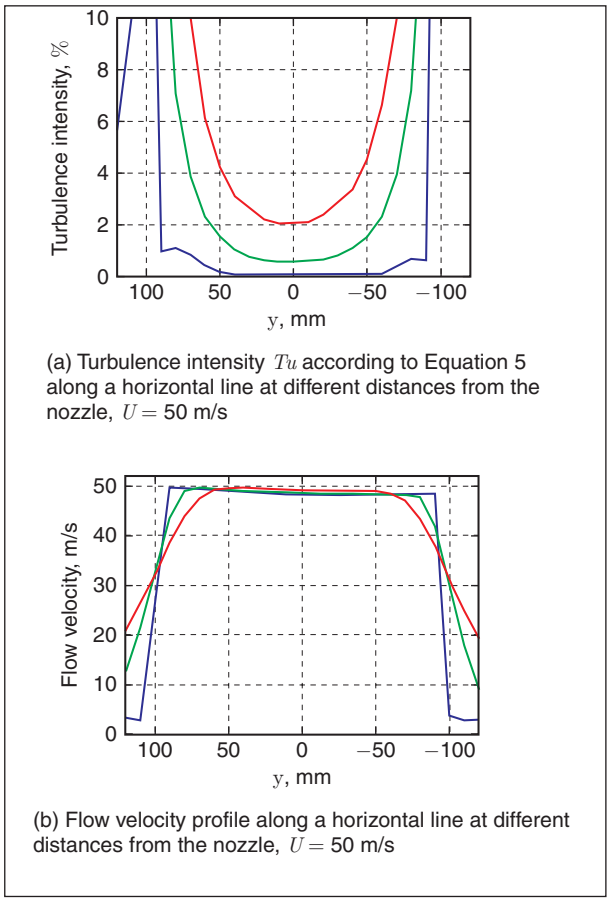

Figure 3. Wind tunnel nozzle characteristics: Turbulence intensity Tu and flow velocity U at three different distances from the nozzle (diameter d = 200 mm): x/d = 0.07, 1, 2.

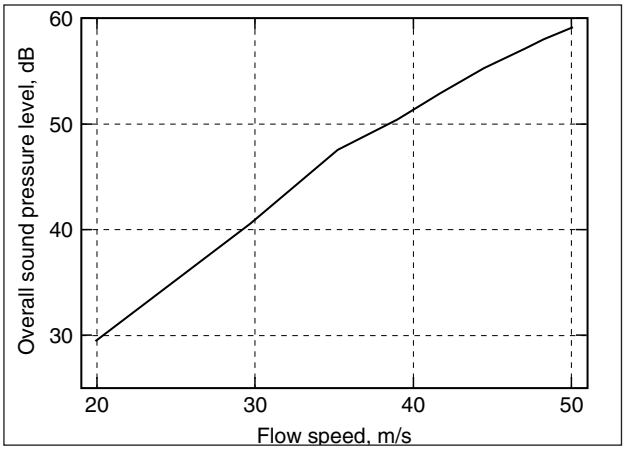

Figure 4. A–weighted overall sound pressure level of the aeroacoustic wind tunnel at a distance of 1 m at 90° to the nozzle axis.

tunnel nozzle. A more detailed description of the aeroacoustic wind tunnel, including extensive data on the wind speed scaling of the wind tunnel self noise, additional turbulence data and a comparison with similar facilities can be found in reference [37].

The airfoil is mounted in the open jet and has a variable angle of attack α. It has to be noted that the results given in the present paper, especially for angles of attack that are not equal zero, cannot be compared to results that would be obtained under free flow conditions. This is due to the coupling of a circular jet with a rectangular,

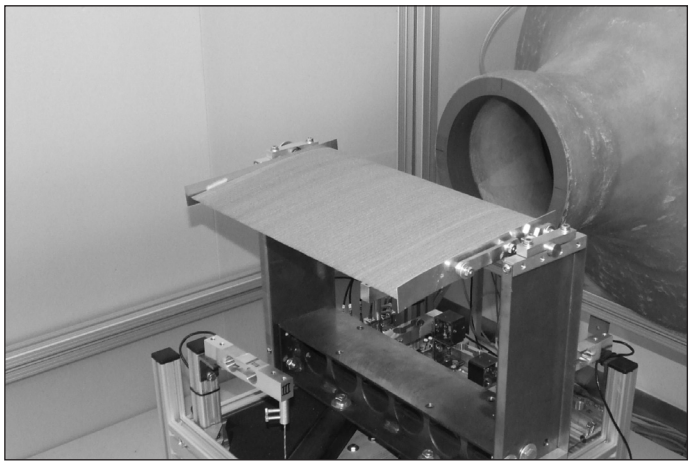

Figure 5. Photograph of a porous airfoil in front of the wind tunnel nozzle.

slightly cambered airfoil and, additionally, to the fact that the airfoils have a very large dimension compared to the wind tunnel nozzle width. This results in different effects like blockage and a variation of the flow field and the loading of the airfoil in the spanwise direction. Therefore, no common methods for the correction of the angle of attack to account for the differences between free flow conditions and the open jet wind tunnel are used here, like those described by Knight and Harris [38] or Brooks et al. [39]. The equations of reference [39] are basically valid for symmetric airfoils only. Nevertheless, for a lack of a more suitable method, those equations are used in the present paper for the calculation of the boundary layer displacement thickness using XFOIL [40] as a means of comparison.

The following coordinate system is used for the description of both acoustic and hot–wire measurements: The x–axis is aligned with the jet axis and y- and z–axis are the horizontal (spanwise) and vertical directions, respectively, their origin being the nozzle exit plane.

2.3. ACOUSTIC MEASUREMENT SETUP

The acoustic measurements were carried out using a planar microphone array with 56 $^1/_4$-inch microphone capsules flush-mounted into a square aluminum plate of 1.5 m $\times$ 1.5 m. The arrangement of the microphones was within two overlapping subgroups of 32 microphones each [41]. However, in the present study all 56 channels were applied simultaneously. The array was located out of flow and 0.68 m above the airfoil (Figure 6).

The width of the main lobe of the microphone array in the array focus plane (at a distance of 0.68 m from the array center) is approximately 0.54 m at 500 Hz, 0.28 m at 1 kHz, 0.14 m at 2 kHz, 0.07 m at 4 kHz, 0.03 m at 8 kHz and in the order of or below 0.015 m at 16 kHz and 0.012 m at 20 kHz.

The data acquisition is achieved by a 24–Bit National Instruments multichannel measurement system, further processing was done using an in-house beamforming code on a cluster of personal computers. Each measurement was conducted with a sample rate of 51.2 kHz and a total of 2,048,000 samples per channel, resulting in 453 MBytes of data per measurement. The effects of the refraction of sound at the shear layer of the wind tunnel on the source localization were estimated prior to the measurements according to reference [42]. The impact on the source localization are relatively small for the described setup and the range of flow speeds used in the experiments. Accordingly, no correction has been used. Another possible effect of the

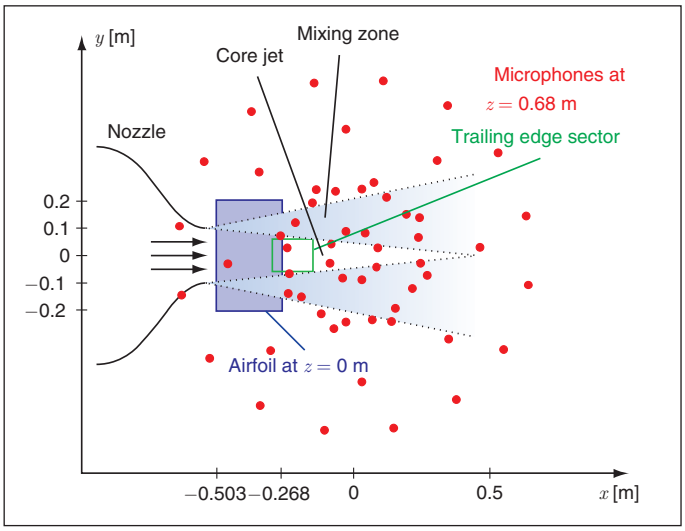

Figure 6. Schematic display of the measurement setup (top view).

shear layer on sound propagation is scattering and subsequent decorrelation. One consequence of this may be a broadening of spectral peaks. In the present study the shear layer is thin and is located in a very small distance from the airfoil (<10 cm). Consequently, this effect should be minimal [43, 44]. Moreover, due to the expected broadband noise characteristics, the possible influence on the results is very small.

2.4. HOT–WIRE MEASUREMENT SETUP

The flow velocity in the turbulent boundary layer of the airfoils was measured using Constant Temperature Anemometry (CTA). The application of a Dantec P15 type boundary layer probe (5 *m*m diameter, 1.25 mm long platinum-plated tungsten wire sensor) with the wire perpendicular to the streamwise velocity component enabled measurements near the surface of the airfoils. The system was calibrated after each measurement using the velocity calibration method (polynomial curve fit) and a Pitot tube. The measured voltage–time–series were transferred by the CTA measurement system in velocity–time–series by using the according calibration equation. The CTA hardware includes a low–pass filter with a cutoff–frequency of 10 kHz. A 24–Bit National Instruments data acquisition system was used to digitize the raw data. The sample frequency was chosen to be 25.6 kHz with a total number of 256,000 samples, leading to a measurement duration of 10 s per measurement point.

The positioning of the probe was done using an ISEL lightweight traversing system with a minimum step size of 0.1 mm.

The hot–wire measurements of the velocity profiles in the vicinity of the airfoils were performed above the airfoil surface and in the wake of the airfoil. The horizontal position (y–direction) of the measurements was approximately at mid–span, inside the core jet of the wind tunnel. Eleven chordwise coordinates (x–coordinates) were chosen above the airfoil and two additional coordinates in the wake of the airfoil. Figure 7 shows the streamwise coordinates of the measurement positions. Thereby, the distance of the x–coordinates from the airfoil trailing edge is 0, -5, -10, -20, -30, -45, -60, -80, -100, -120 and -140 mm (corresponding to approximately 0, 2.1, 4.3, 12.7, 19.1, 25.5, 34.0, 42.6, 51.1 and 59.6 % of the chord) towards the leading edge and the distance of the measuring points in the wake is +1 and +5 mm

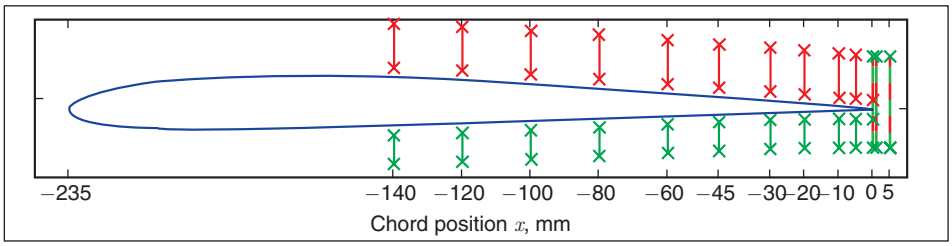

Figure 7. Positions for the CTA boundary layer measurements (eleven chordwise positions and two positions in the wake–region), given is the path in the x–z–plane along which each 52 measurements were made (red color denotes the paths on the suction side, green the paths on the pressure side of the airfoil).

(0.4, 2.1 % of the chord). At least 52 measurement positions were located in the vertical (z-) direction for the measurement of the velocity profiles of the boundary layer (at every chord station on one side of the airfoil) and twice this number for the velocity measurements at the stations in the wake of the airfoil. The distance between measurement points in the vertical direction was varied: Directly above the surface, the step size was chosen to be the minimum step size of 0.1 mm, while with increasing distance from the surface the step size changed to 0.2 mm and finally to 1 mm. This led to a total of nearly 800 measurements for one side of the airfoil at one flow speed U and one angle of attack. For some of the test series, this number was exceeded.

Common procedures used to determine the distance between the hot–wire and the surface of the airfoil like the Clauser plot method [45] or methods using the cooling of the wire near the surface of a (non–porous) airfoil were of no use in the described experiments. One reason is that, contrary to the theoretical flow conditions assumed for non–porous airfoils (the *law of the wall* [46]), no theory for the conditions at the surface of flow–permeable airfoils is available. The assumption of a flow velocity of $u(z = 0) = 0$ as a fixed boundary condition can not be made due to a presumable flow inside the porous material. Additionally, the surface of the porous airfoils is not smooth and two of the porous airfoils are made of a metallic material and are therefore electrically conductive. Due to these reasons a more approximate and time consuming method had to be used instead for the measurements on porous airfoils: A dummy sensor with exactly the same geometry as the hot–wire probe (simply another Dantec P15 boundary layer probe without the Tungsten wire) was used to optically determine the vertical position when the prongs just touched the surface of the airfoil. Thus, the absolute accuracy of the vertical (z) position of the hot–wire probe is at the maximum equivalent to that of the traversing system (0.1 mm).

3. DATA PROCESSING

3.1. ACOUSTIC DATA

The raw data of the 56 microphones were further processed on a cluster of personal computers to obtain the trailing edge noise spectra. The sampled microphone signals were transformed using a Fast Fourier Transformation (FFT) with a Hanning window and 4,096 samples per block, giving a total of 999 blocks with an overlap of 50%. The resulting $56^2 = 3{,}136$ cross spectra were calculated and averaged to obtain the cross spectral matrix.

Three advanced beamforming algorithms were tested on the data: the orthogonal beamforming (OB) method

[47], the deconvolution approach for the mapping of acoustic sources (DAMAS) [48] and the CLEAN-SC beamforming method [49]. The DAMAS algorithm gives good results especially for low frequencies, where it localizes noise sources at the expected positions. The orthogonal beamforming method was found to deliver the most reliable results at higher frequencies, where the CLEAN–SC in some cases failed to locate sound sources and the DAMAS algorithm tended to overestimate the emitted noise for some of the porous airfoils. The result of the beamforming are spatial images of the local sound pressure contributions called sound maps (similar to "acoustic photographs").

Figure 8 shows a comparison of four beamforming algorithms, a conventional delay-and-sum algorithm, the orthogonal beamforming algorithm (utilizing 36 eigenvalues), the DAMAS algorithm and the CLEAN–SC algorithm, for the non–porous reference airfoil by means of octave band sound maps. It can be seen that although basically the different algorithms deliver comparable results regarding the source position, the source strengths differ. The differences between the results of the orthogonal

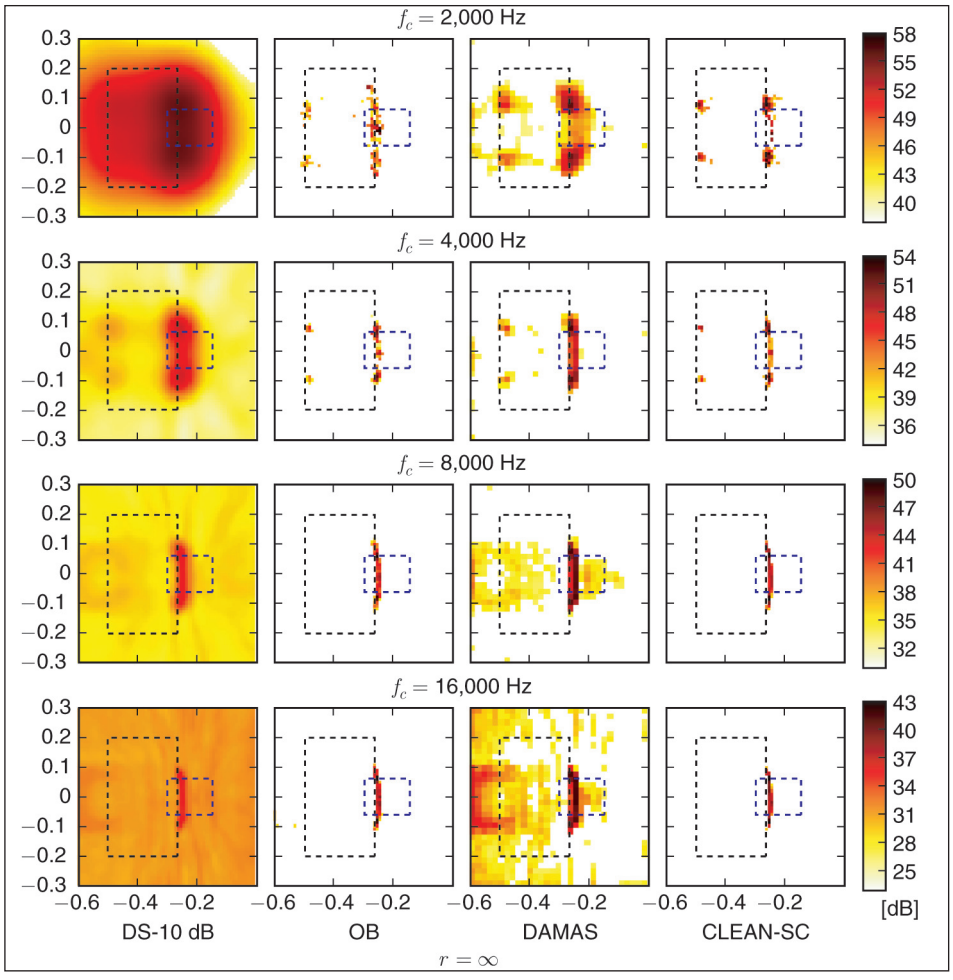

Figure 8. Comparison of different beamforming algorithms (from left to right: delay-and-sum, orthonal beamforming, DAMAS, CLEAN–SC) for the non–porous reference airfoil, U = 50 m/s, α = 0°, octave band sound maps, center frequencies indicated (dotted black line: airfoil, dotted blue line: integration sector). The results of the delay-and-sum algorithm are reduced by 10 dB to enable a better comparison with the remaining algorithms.

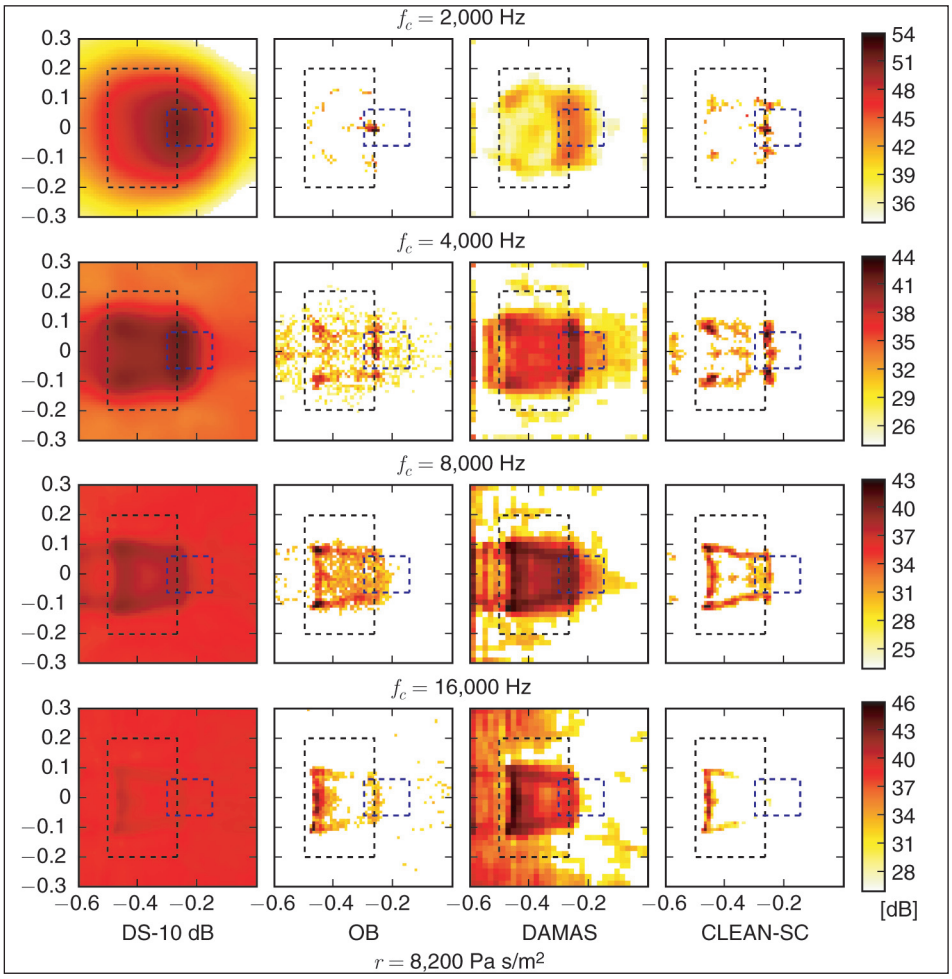

Figure 9. Comparison of different beamforming algorithms (from left to right: delay-and-sum, orthonal beamforming, DAMAS, CLEAN–SC) for one porous reference airfoil (Recemat, r = 8,200 Pa s/m^2) U = 50 m/s, α = 0°, octave band sound maps, center frequencies indicated (dotted black line: airfoil, dotted blue line: integration sector). The results of the delay-and-sum algorithm are reduced by 10 dB to enable a better comparison with the remaining algorithms.

beamforming, the DAMAS and the CLEAN–SC are relatively small for the non–porous airfoil. However, Figure 9 shows the comparison of the same algorithms for one porous airfoil (Recemat, r = 8,200 Pa s/m^2). In this case the differences regarding source position and source strength are more obvious, especially at higher frequencies. In the 16 kHz octave band for example the DAMAS algorithm localizes noticeable noise sources in the trailing edge sector, whereas the maximum source strength calculated using the orthogonal beamforming method is clearly below the DAMAS result. The CLEAN–SC result is even below that of the orthogonal beamforming and, given the chosen dynamic range of the plot, hardly visible in the according sound map. A comparison of third octave band sound pressure level spectra derived on the basis of the different beamforming algorithms for several airfoils is given in [8].

Due to these reasons all acoustic results throughout the remaining paper were calculated using the DAMAS algorithm for low frequency noise components below the 4 kHz third octave band, while the orthogonal beamforming algorithm was used for frequencies above the 3.15 kHz third octave band. The spatial resolution of the map used for the orthogonal

beamforming was 0.01 m for a map of 0.6 m in x-direction by 0.8 m in y-direction (see Figure 6). The spatial resolution of the DAMAS beamforming algorithm was set to 0.02 m for the identical map due to the substantial computational cost and the long calculation period.

Absolute sound pressure levels were obtained by integration of the resulting beamfoming map over the accordant noise source region. Since this paper focuses on the generation of noise at the trailing edge and its correlation with the turbulent boundary layer, the sector chosen for the integration of the sound maps contains only the central trailing edge region of the airfoil. It has a width of 0.12 m (in spanwise direction) and can be seen in Figure 6. The airfoil leading edge and the lateral edge regions as well as the impingement region of the shear layers are not located in this sector.

The resulting spectra of the power spectral density (*PSD*) were then transferred to third–octave–band spectra of the sound pressure level (*SPL*) with center frequencies between 1.6 kHz and 20 kHz. For some analyses, the overall sound pressure level *OASPL* was calculated based on the resulting third–octave–band sound pressure levels. The *OASPL* in this research is calculated as a summation of the third octave band sound pressure levels SPL_i with center frequencies between 1.6 kHz and 20 kHz (in agreement with Equation 1):

$$OASPL = 10 \cdot log_{10}\left(\sum_{f_m=1.6\,\mathrm{kHz}}^{20\,\mathrm{kHz}} 10^{[SPL_i/(10\,dB)]}\right)\ \mathrm{dB} \qquad (6)$$

The omission of low frequency noise contributions to the *OASPL* is a limitation, since this low frequency noise contains a noticeable fraction of the overall sound energy. However, in order to focus on the trailing edge noise generation this separation of the high frequency noise contributions is necessary using the described measurement setup to ensure the non–compactness condition of the airfoil according to Equation 1. This omission of the low frequency noise contributions is important when discussing the measured *OASPL*.

3.2. HOT–WIRE DATA

The processing of the hot–wire data was realized using self–developed code. The input for the calculations were the time–discrete velocity data acquired by the 24–Bit National Instruments system (velocity–analysis method [50]). Although a very low traversing speed of 10 mm/s was chosen, slight vibrations of the probe shortly after each step of the traversing system cannot be prevented. To counteract this effect, the first two seconds of every measured time series were omitted before the further procession of the CTA data. The remaining time domain data were then transferred to the frequency domain by using an FFT with a Hanning window and 4,096 samples per block. A high–pass–filter with a cutoff–frequency of 10 Hz was used to eliminate the offset velocity and the low–frequency–turbulence contributions from the wind tunnel that are not generated at the airfoils.

To characterize the turbulent flow over the trailing edge in an incompressible flow, four different statistical flow parameters were calculated from the distribution of the mean velocity $u(z)$ (according to reference [51]):

- the boundary layer thickness δ, as the vertical distance from the airfoil surface, where the mean velocity reaches 99% of the outer velocity,
- the boundary layer displacement thickness

$$\delta_1 = \int_{z=0}^{\infty}\left(1-\frac{(u(z)}{U}\right)dz, \qquad (7)$$

- the momentum thickness

$$\delta_2 = \int_{z=0}^{\infty} \left(1 - \frac{(u(z)}{U}\right) \cdot \left(\frac{(u(z)}{U}\right) dz \quad (8)$$

and

- the energy thickness

$$\delta_3 = \int_{z=0}^{\infty} \left[1 - \left(\frac{(u(z)}{U}\right)^2\right] \cdot \left(\frac{(u(z)}{U}\right) dz. \quad (9)$$

The integration in Equation 7 through 9 was implemented using the trapezoidal rule.

4. RESULTS AND DISCUSSION

4.1. AEROACOUSTIC RESULTS

The aeroacoustic measurements were conducted at 15 flow speeds ranging approximately from 26 m/s to 50 m/s. This resulted in ranges of the Mach number from approximately 0.08 to 0.15 and the chord based Reynolds number from $4 \cdot 10^5$ to $8 \cdot 10^5$. The geometric angle of attack was varied between -20° and 24° in steps of 4°.

Figure 10 and Figure 11 show the octave band sound maps, obtained using the beamforming algorithms described in Section 3.1. To enable comparisons between the sound maps of the four

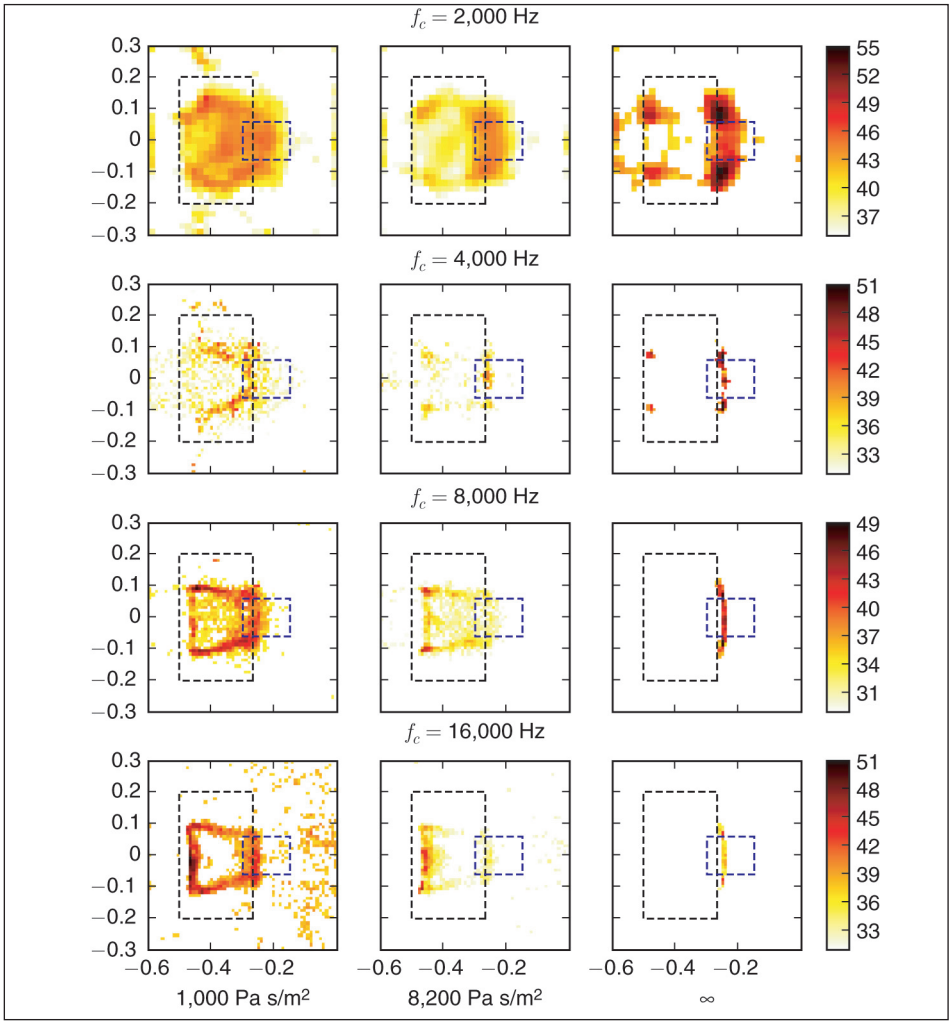

Figure 10. Octave band sound maps of two porous airfoils (r = 1,000 Pa s/m² and r = 8,200 Pa s/m²) and the non-porous airfoil, U = 50 m/s, α = 0°, center frequencies indicated (dotted black line: airfoil, dotted blue line: integration sector). The 2 kHz octave band sound map was calculated using the DAMAS beamforming algorithm and the remaining sound maps were calculated using the orthogonal beamforming.

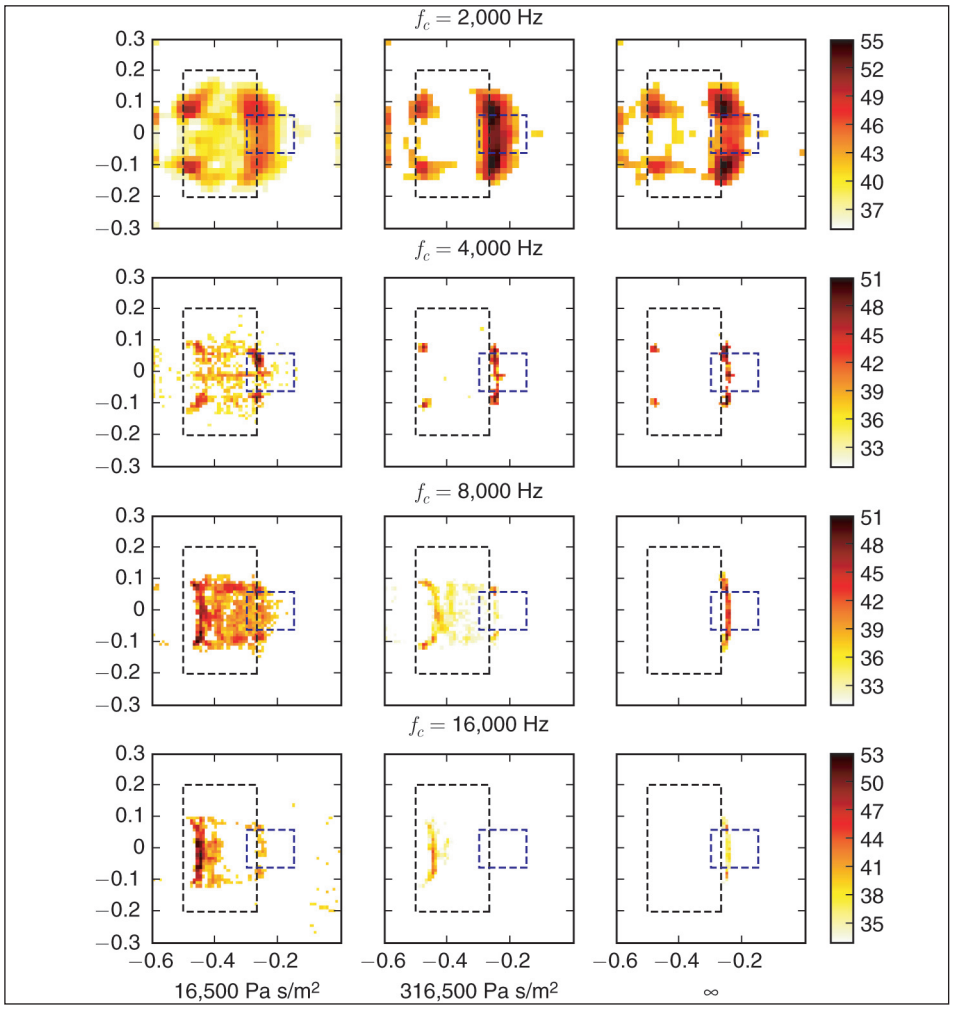

Figure 11. Octave band sound maps of two porous airfoils (r = 16,500 Pa s/m² and r = 316,500 Pa s/m²) and the non-porous airfoil, U = 50 m/s, α = 0°, center frequencies indicated (dotted black line: airfoil, dotted blue line: integration sector). The 2 kHz octave band sound map was calculated using the DAMAS beamforming algorithm and the remaining sound maps were calculated using the orthogonal beamforming.

porous airfoils and the non–porous reference airfoil, the latter is given in both Figure 10 and 11. The sound maps show that the noise source regions of the porous airfoils compared to the reference airfoil differ depending on the frequency. For higher frequencies a clear trend is visible that the major noise sources of the porous airfoils are shifted towards the airfoil leading edge. This seems reasonable since the porous airfoils have very rough surfaces that the non–porous reference airfoil has not.

Figure 12 shows the scaled third octave band sound pressure level for each of the five

airfoils listed in Table 1 as a function of the chord based Strouhal number $Sr = \frac{f \cdot c_l}{U}$.

The scaling was done using Equation 3. The scaling approach was found to give the best results for the non–porous reference airfoil when the exponent n was chosen to equal 4.6, which was subsequently used also for the porous airfoils to enable a better comparison. It can be seen from the figure that this scaling seems to be valid for the reference airfoil, because the resulting curve shows no considerable

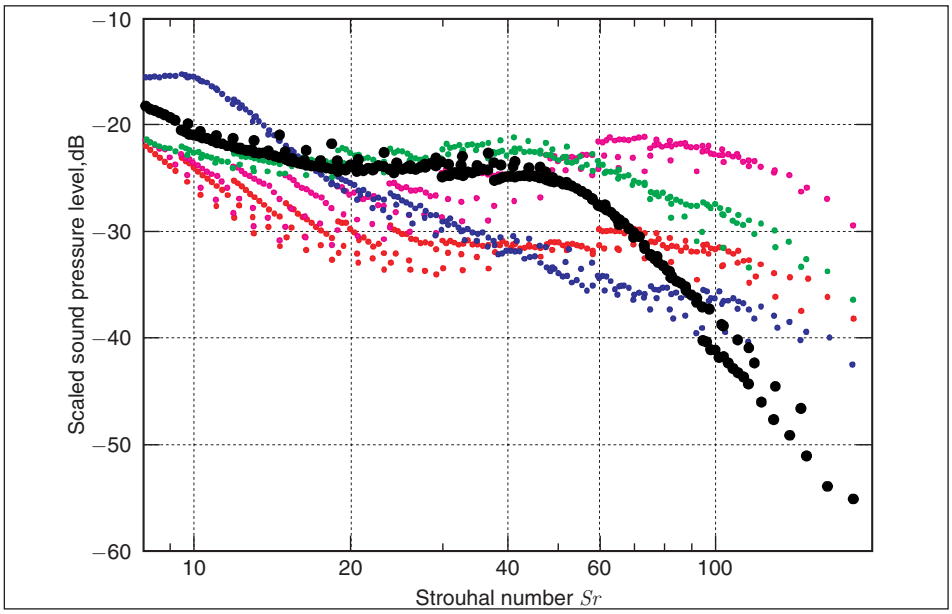

Figure 12. Overview of the sound pressure level, scaled using Equation 3 with n = 4.6, as a function of the chord based Strouhal number Sr at α = 0°, different colors denote different porous materials, bigger black dots indicate the non–porous airfoil (r = ∞, 316,500, 16,500, 8,200, 1,000 Pa s/m^2).

dependency on other degrees of freedom. However, this scaling approach is not valid without restrictions for the porous airfoils, although it might be a good first guess for some of them. An appropriate scaling approach that is adapted to the porous material parameters is not available yet.

Figure 13(a) shows the dependency of the overall sound pressure level of the four porous and the non–porous airfoil on the flow speed U . It reveals that the overall sound pressure level clearly depends on the flow speed U in the examined range of flow speeds. For increasing flow speeds the overall sound pressure level increases. The *OASPL* of the airfoil made of Recemat (r = 8,200 Pa s/m^2) is very low compared to the other airfoils, which corresponds to the according sound maps given in Figure 10. However, when discussing the measured *OASPL* the restrictions of the calculation procedure, namely the omission of the low frequency noise components as discussed in Section 3.1, have to be kept in mind. Figure 13(b) gives the overall sound pressure level as a function of the geometric angle of attack α. For the data processing of the measurements at angles of attack not equal to zero, the original distance of the array focus plane of 0.68 m (see Figure 6) was adjusted according to the exact trailing edge position. It can be seen that in general the dependency of the *OASPL* measured at the airfoil trailing edge on the angle of attack is more complex than the dependency on the flow speed. For some of the airfoils (non–porous airfoil, $r = \infty$, and Porex, r = 316,500 Pa s/m^2) it is rather small, at least for the range of angles examined in the present research with the exception of -12° angle of attack. At this angle, the *OASPL* of the non–porous airfoil is higher than for the other angles. For the airfoil made of Recemat (r = 8,200 Pa s/m^2) the overall sound pressure level increases when the absolute value of the geometric angle of attack increases, which is, although somewhat less distinctive, also true for the airfoils made of M–Pore Al 45 ppi (r = 1,000 Pa s/m^2) and Reapor (r = 16,500 Pa s/m^2).

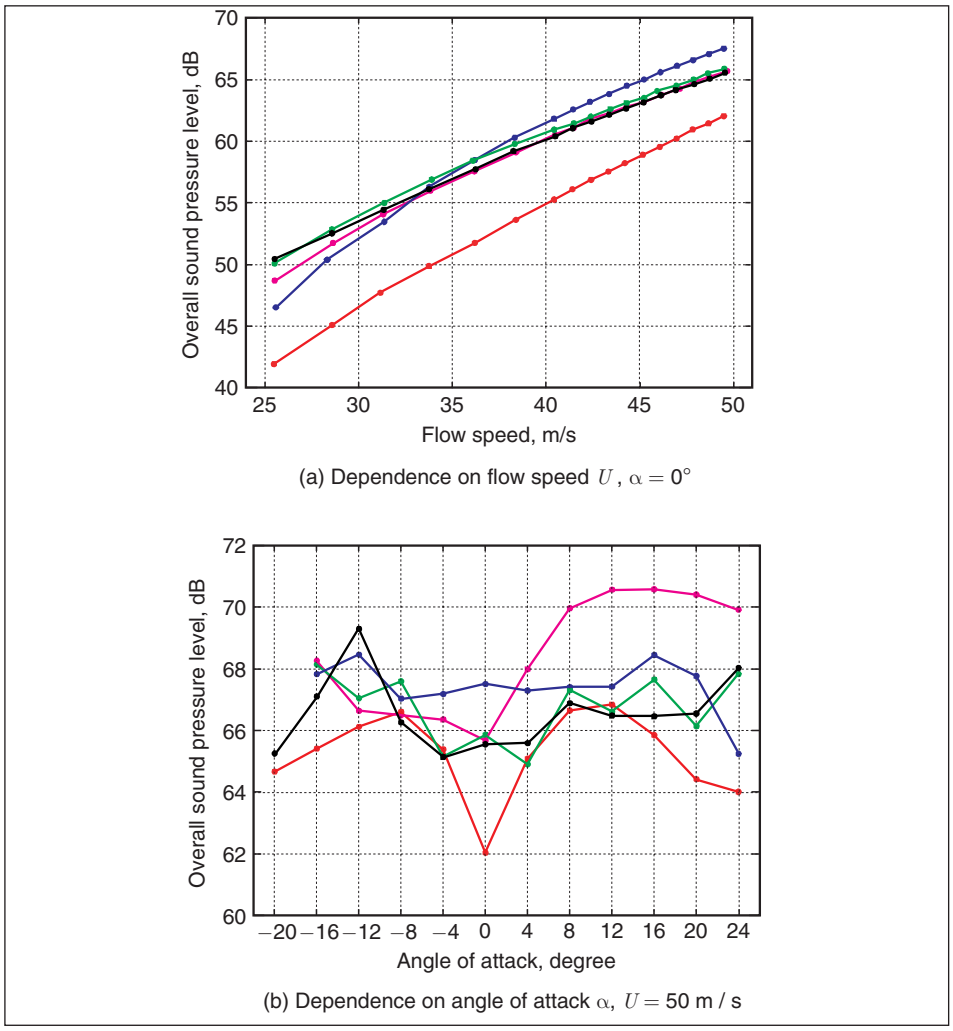

Figure 13. Dependence of the overall sound pressure level SPL on flow speed U and (geometric) angle of attack α (r = ∞, 316,500, 16,500, 8,200, 1,000 Pa s/m^2).

The spectral shapes of the third octave band sound pressure levels of the porous airfoils are different from each other and from that of the reference airfoil. Figure 14 shows the frequency dependence of the third octave band sound pressure level *SPL* generated at the trailing edge of the airfoils. The *SPL* measured for the airfoil made of Reapor (r = 16,500 Pa s/m^2) exceeds the *SPL* of the non–porous airfoil for frequencies greater than 2.5 kHz. One possible reason might be the trailing edge of the Reapor airfoil. The airfoil itself is made out of porous glass pellets and therefore it is very fragile. Due to some of the pellets breaking out during the assembling of the airfoil, its trailing edge at some spanwise positions is not as even as those of the other airfoils. This might be the source of the increased trailing edge noise generation compared to the non–porous airfoil. At low frequencies (below approximately 3 kHz) only the *SPL* of the porous airfoil made of Porex (r = 316,500 Pa s/m^2) exceeds the *SPL* of the non–porous airfoil, while with increasing frequency the *SPL* of the Porex airfoil strongly decreases. For high frequencies above approximately 6 kHz, the *SPL* of the airfoils made of M–Pore Al 45 ppi (r = 1,000 Pa s/m^2) exceeds the *SPL* of the non–porous airfoil. At very high frequencies, especially visible in the 20 kHz third octave band, all porous airfoils generate more noise than the non–porous airfoil.

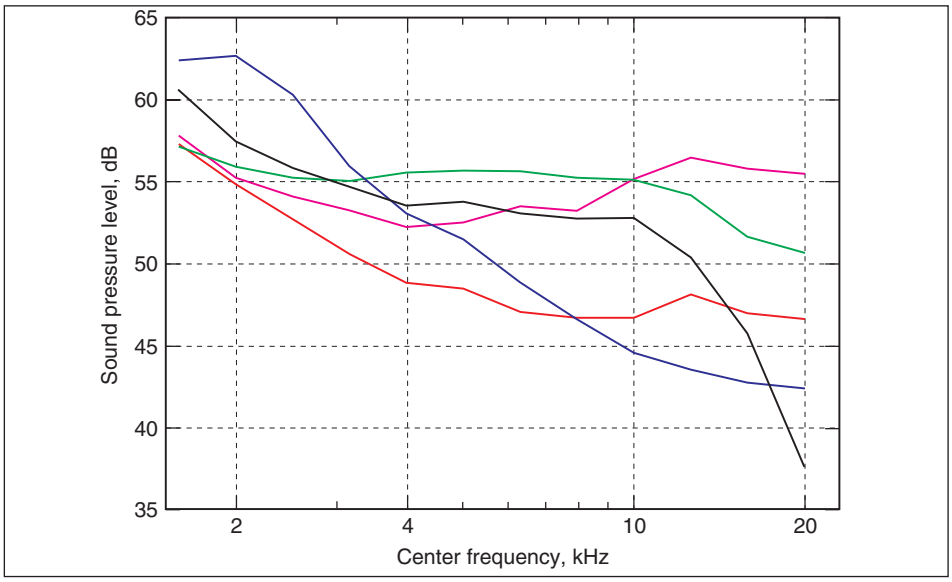

Figure 14. Resulting sound pressure level at α = 0° and U = 50 m/s (r = ∞, 316,500, 16,500, 8,200, 1,000 Pa s/m²).

In general, a noticeable noise reduction can be achieved over a large range of medium frequencies for nearly all of the porous airfoils compared to the reference airfoil, the maximum of the noise reduction being in the order of 8 dB.

Interestingly, the influence of the increased trailing edge thickness of the porous airfoils, the *trailing edge bluntness noise*, which usually (for non–porous airfoils) results in a noticeable spectral peak, can not be distinctively recognized in Figure 14. The spectral peak due to the bluntness noise contribution of the non–porous airfoil with a trailing edge thickness of 0.5 mm can be detected from Figure 14 between approximately 10 kHz and 12 kHz. According to the BPM–model, this peak frequency shifts to lower frequencies for an increasing trailing edge thickness (for a constant chord length and unchanged airfoil shape). The bluntness noise contribution for the porous airfoils with a trailing edge thickness of 1.59 mm should therefore be visible at a frequency clearly below 10 kHz. But since no noticeable narrowband peak appears in the third octave band sound pressure level spectra of the porous airfoils, the influence of the bluntness noise contribution on the emitted trailing edge noise may be negligible.

The porosity of the examined airfoils is in each case accompanied by a certain roughness of the airfoil surface which results in a contribution of surface roughness noise to the overall trailing edge noise. But the acoustic results show that a noticeable trailing edge noise reduction is possible through the use of porous materials despite the presumable contribution of surface roughness noise. Hence, the noise reducing effect of the porosity of the airfoils seems to have a bigger impact on the overall trailing edge noise than the surface roughness. Nevertheless, the high frequency noise contribution of the porous airfoils that is visible in Figure 14 (20 kHz third octave band) and, consequently, in Figure 12, might be originating from the surface roughness of the porous airfoils. The sound maps given in Figure 10 and 11 further confirm this theory. Additionally, this assumption seems to be supported by the fact that the high frequency noise emission of the porous airfoils from Figure 14 increases for decreasing flow resistivities of the porous materials. The airfoils with the highest sound pressure levels at high frequencies are (in descending order)

M–Pore Al 45 ppi (r = 1,000 Pa s/m^2), Reapor (r = 16,500 Pa s/m^2) and Recemat (r = 8,200 Pa s/m^2). Apparently, porous airfoils made of materials with relatively low flow resistivities (and bigger pores) would therefore exhibit a higher surface roughness than airfoils made from materials with a high flow resistivity (and small pores). In this case, further research is necessary to fully understand the influence of the surface roughness of the porous airfoils on the overall trailing edge noise emission.

4.2. BOUNDARY LAYER RESULTS

For the five airfoils from Table 1 hot–wire measurements were carried out at a mean flow speed of approximately 50 m/s and a geometric angle of attack of 0° at the positions indicated in Figure 7. For the porous airfoil made out of Recemat (r = 8,200 Pa s/m^2) and the non–porous airfoil, further measurements were done above the trailing edge (at x = 0) for varying flow speeds to capture the influence of the mean flow speed U on the generation of the turbulent boundary layer. Additional measurements were done for different angles of attack a on selected airfoils in order to understand the influence of the angle of attack on the turbulent boundary layer. The influence of the spanwise position y on the measured boundary layer properties has been tested in preliminary experiments and was found to be negligible when inside the virtually non–turbulent core jet of the wind tunnel. Outside this core jet, the shear layer and the turbulent mixing zone of the free jet (see Figure 6) heavily affect the results of the CTA. Hence, all hot–wire measurements described in this paper were carried out inside the wind tunnel core jet with negligible deviations from the nozzle axis in the y–direction.

Figure 15 through 19 show the velocity profiles measured at the surfaces of the non–porous airfoil and the four porous airfoils. The upper portion of each figure presents the velocity profiles of the suction side of the airfoil, the lower portion that of the pressure side. The eleven chordwise positions and the two positions in the wake– region for each measurement series are those given in Figure 7. The two rightmost measurement positions (the two rightmost lines in each figure) were located 1 mm and 5 mm behind the trailing edge of each airfoil. The figures provide a qualitative overview of the different turbulent boundary layer

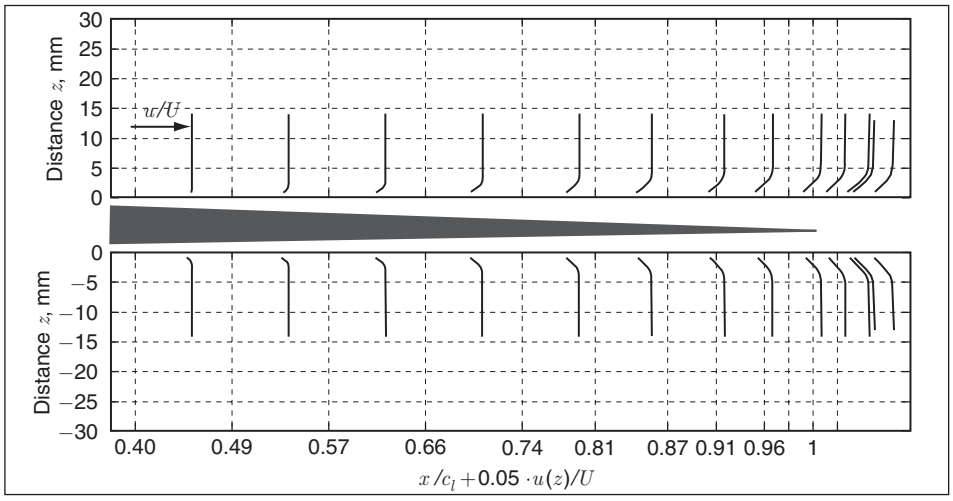

Figure 15. Measured velocity profiles at suction- (upper figure) and pressure-side (lower figure) of the airfoils, α = 0° and U = 51 m/s, non-porous airfoil, $r = \infty$.

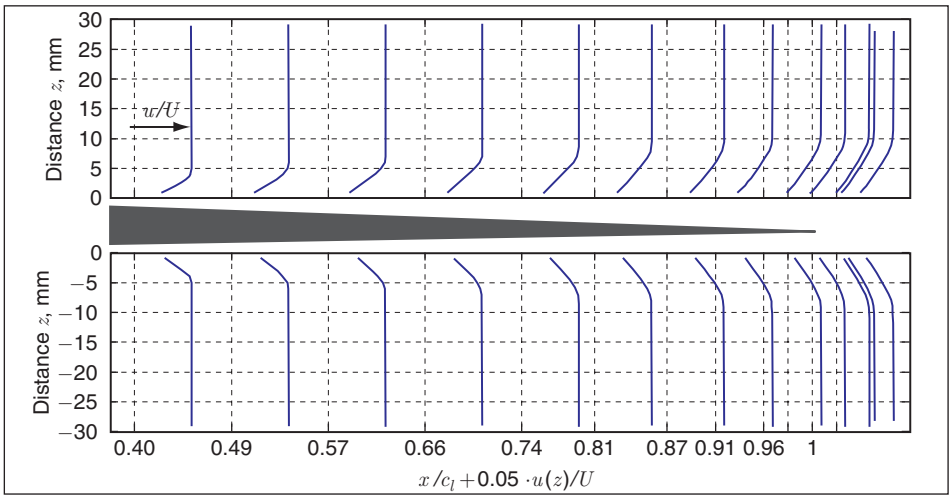

Figure 16. Same as Figure 15, Porex, r = 316.500 Pa s/m^2.

thicknesses. The quantitative boundary layer properties are given in the following diagrams. However, it is clearly visible from Figures 15 through 19 that the turbulent boundary layers of the porous airfoils are thicker than that of the reference airfoil. Furthermore, the boundary layer thickness seems to increase for decreasing flow resistivities of the porous material (from Figure 15 to Figure 19) for both suction and pressure side.

The velocity profiles measured in the wake of the airfoils are presented in Figure 20. Figure 20(a) gives the velocity profiles measured 1 mm behind the trailing edge of the airfoils. As also shown in Figure 15 through 19 it can be seen from these velocity profiles that with decreasing flow resistivity *r* the boundary layer thickness increases. At the pressure side ($z < 0$) the sequence of the measured boundary layer thicknesses (from lower to higher values: non–porous airfoil, Porex, Reapor, Recemat, M–Pore) is exactly consistent with the reversed order of the flow resistivities *r* of the according porous materials. At the suction side ($z > 0$) the boundary layer thickness of the airfoil made of Porex (r = 316,500 Pa s/m^2) is smaller than that of the airfoil made of Reapor (r = 16,500 Pa s/m^2), despite its higher flow resistivity. This effect has to be further analyzed. Figure 20(b) then shows the velocity profiles at a position 5 mm behind the trailing edge of the airfoils. Both Figure 20(a) and 20(b) implicate that, despite a presumed flow inside the porous

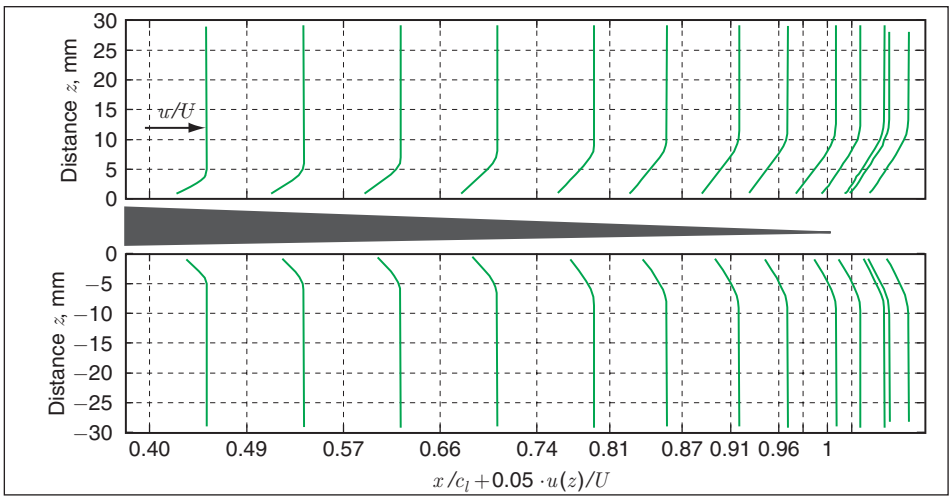

Figure 17. Same as Figure 15, Reapor, r = 16,500 Pa s/m^2.

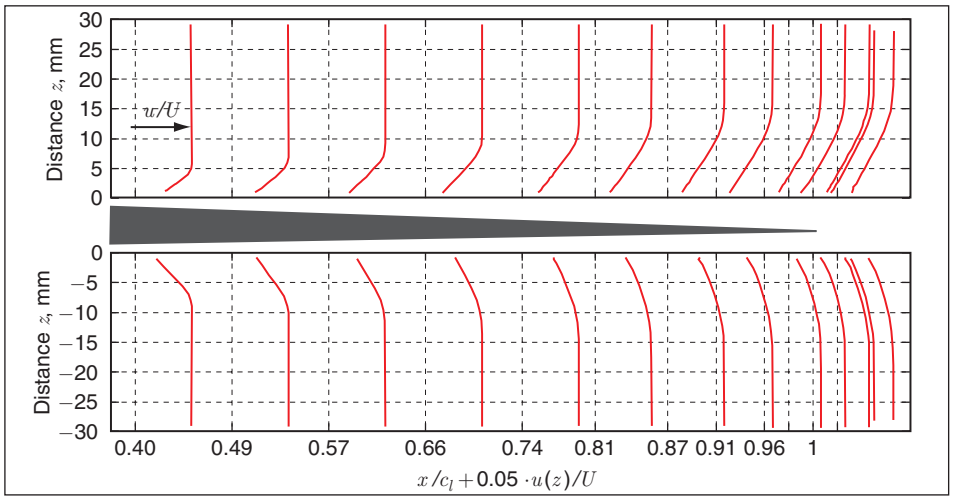

Figure 18. Same as Figure 15, Recemat, r = 8,200 Pa s/m^2.

materials, the velocity directly at the surface of the airfoil (z = 0) is very small, although not necessarily equal zero. Interestingly, the porous consistency of the materials has an influence on the wake behind the trailing edge, as can be seen in Figure 20(b). This is especially visible for the airfoil made of M–Pore Al 45 ppi, the material with the lowest flow resistivity of 1,000 Pa s/m^2, where a noticeable increase of the flow velocity directly behind the trailing edge was measured.

The statistical flow parameters of the turbulent boundary layers (displacement thickness, momentum thickness and energy thickness) calculated with Equation 7 through 9, are presented in Figure 21(a), 21(b) and 21(c), respectively. The boundary layer displacement thickness δ_1 of the porous airfoils is considerably greater than that of the non–porous reference airfoil (see Figure 21(a)) for both suction side and pressure side. For the airfoil with the lowest flow resistivity (M–Pore Al 45 ppi, r = 1,000 Pa s/m^2) the greatest boundary layer displacement thickness was measured while for the two porous airfoils with the highest flow resistivities, namely Porex (r = 316,500 Pa s/m^2) and Reapor (r = 16,500 Pa s/m^2), the smallest displacement thicknesses of the porous airfoils have been determined. And while the displacement thicknesses for the suction side and pressure side of the non–porous airfoil seem to be very similar, it differs noticeably for the porous airfoils. A possible reason for

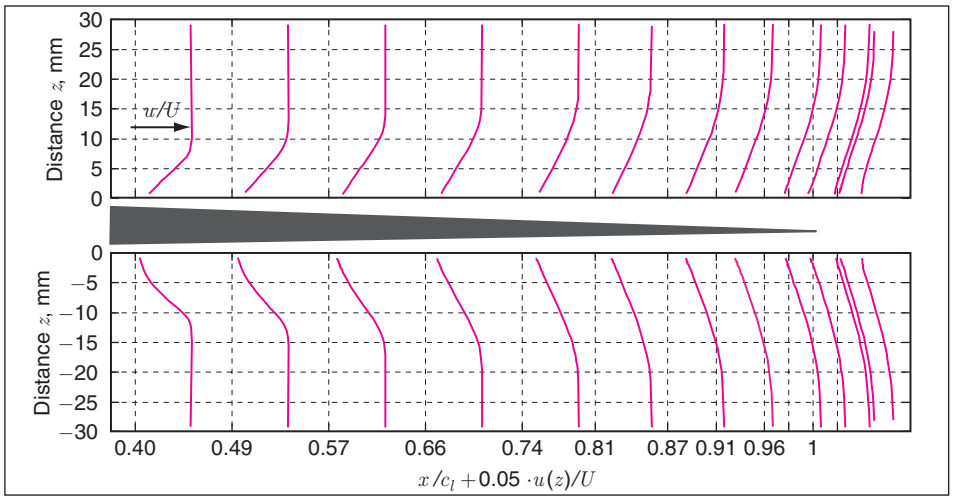

Figure 19: Same as Figure 15, MPore, r = 1,000 Pa s/m^2.

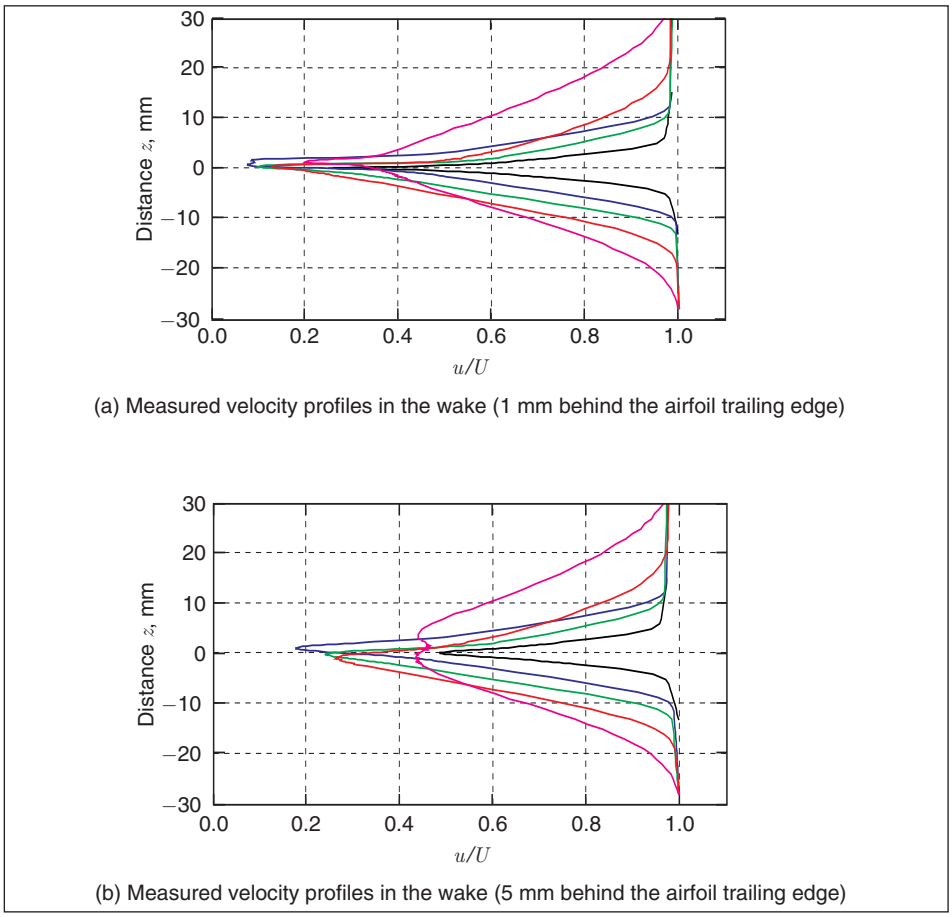

(a) Measured velocity profiles in the wake (1 mm behind the airfoil trailing edge)

(b) Measured velocity profiles in the wake (5 mm behind the airfoil trailing edge)

Figure 20. Measured velocity profiles in the wake, α = 0° and U = 51 m/s (r = ∞, 316,500, 16,500, 8,200, 1,000 Pa s/m²). Note that the given distance in the vertical direction relates to the upper side of the trailing edge.

this difference might be a fluid flow through the porous airfoils. The order of the airfoils regarding their generated turbulent boundary layer displacement thickness in general seems to be similar to that found in Figure 20 and Figures 15 through 19: For decreasing flow resistivities, the displacement thickness apparently increases. This is indeed true for the displacement thickness measured at the suction side. For the boundary layer displacement thickness of the pressure side there is only one exception: The displacement thickness of the airfoil made of Reapor (r = 16,500 Pa s/m^2) is smaller than that of the airfoil made of Porex (r = 316,500 Pa s/m^2), despite the lower flow resistivity of the latter material. For validation purposes, the boundary layer displacement thickness of a non–porous SD7003–shaped airfoil with the same chord length of 235 mm was calculated directly at the trailing edge position on both suction and pressure side using XFOIL. The results are included in Figure 21(a). The measured displacement thicknesses of the reference airfoil are somewhat below that calculated, but this deviation between theory and measurement seems acceptable when the more approximate procedure to determine the distance between hot–wire and airfoil surface (as described in the setup of the hot–wire measurements) is kept in mind.

The results of the calculation of the boundary layer momentum thickness, Figure 21(b), and the energy thickness, Figure 21(c), are consistent to those of the displacement thickness: With decreasing flow resistivities, the

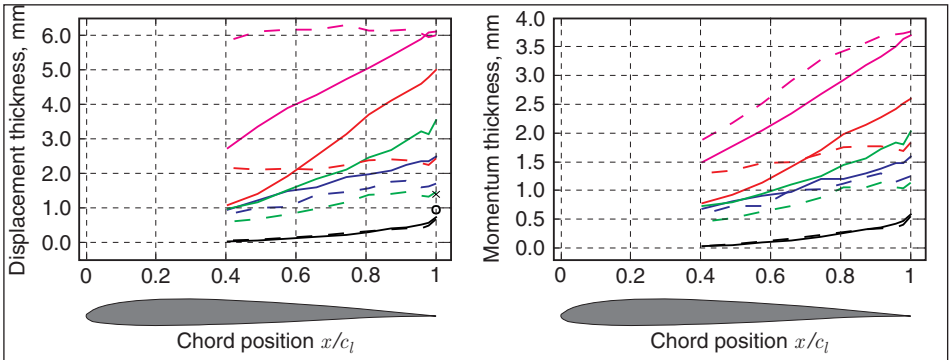

(a) Boundary layer displacement thickness, calculated using Equation 7 (the "x" and "o" denote the displacement thickness calculated using XFOIL for suction side and pressure side, respectively.)

(b) Boundary layer momentum thickness, calculated using Equation 8

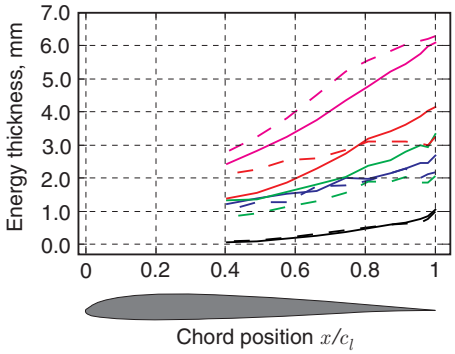

(c) Boundary layer energy thickness, calculated using Equation 9

Figure 21. Statistic flow parameters, α = 0° and U = 51 m/s, the continuous line represents the results from the suction side, the dashed line those from the pressure side of each airfoil (r = ∞, 316,500, 16,500, 8,200, 1,000 Pa s/m²). Note that the schematic of the airfoil is given for illustrative purpose only, the distance given on the ordinate refers to the airfoil surface as origin.

momentum thickness as well as the energy thickness decreases. This is especially true for the measurements at the suction side. At the pressure side, however, the porous material with the second highest flow resistivity (Reapor, r = 16,500 Pa s/m²) generates the lowest momentum thickness and energy thickness of the porous materials.

The influence of the mean flow velocity U on the boundary layer displacement thickness δ_1 is shown in Figure 22(a) for the reference airfoil and the porous airfoil made of Recemat (r = 8200 Pa s/m²). Again, the boundary layer displacement thickness calculated for the non–porous airfoil using XFOIL is included in the figure. And while δ_1 slightly increases with increasing flow speed U in both measured cases, it slightly decreases for the calculation. But again, the difference between measured and calculated displacement thickness of the non–porous airfoil is acceptable due to the reasons mentioned above.

The dependence of δ_1 on the angle of attack is given in part in Figure 22(b) for three geometric angles of attack (0°, +4° and +8°) and only a subset of the porous airfoils. It is clearly visible that the angle of attack has a strong influence on the boundary layer displacement thickness of the porous airfoils, while its influence is barely visible for the reference airfoil.

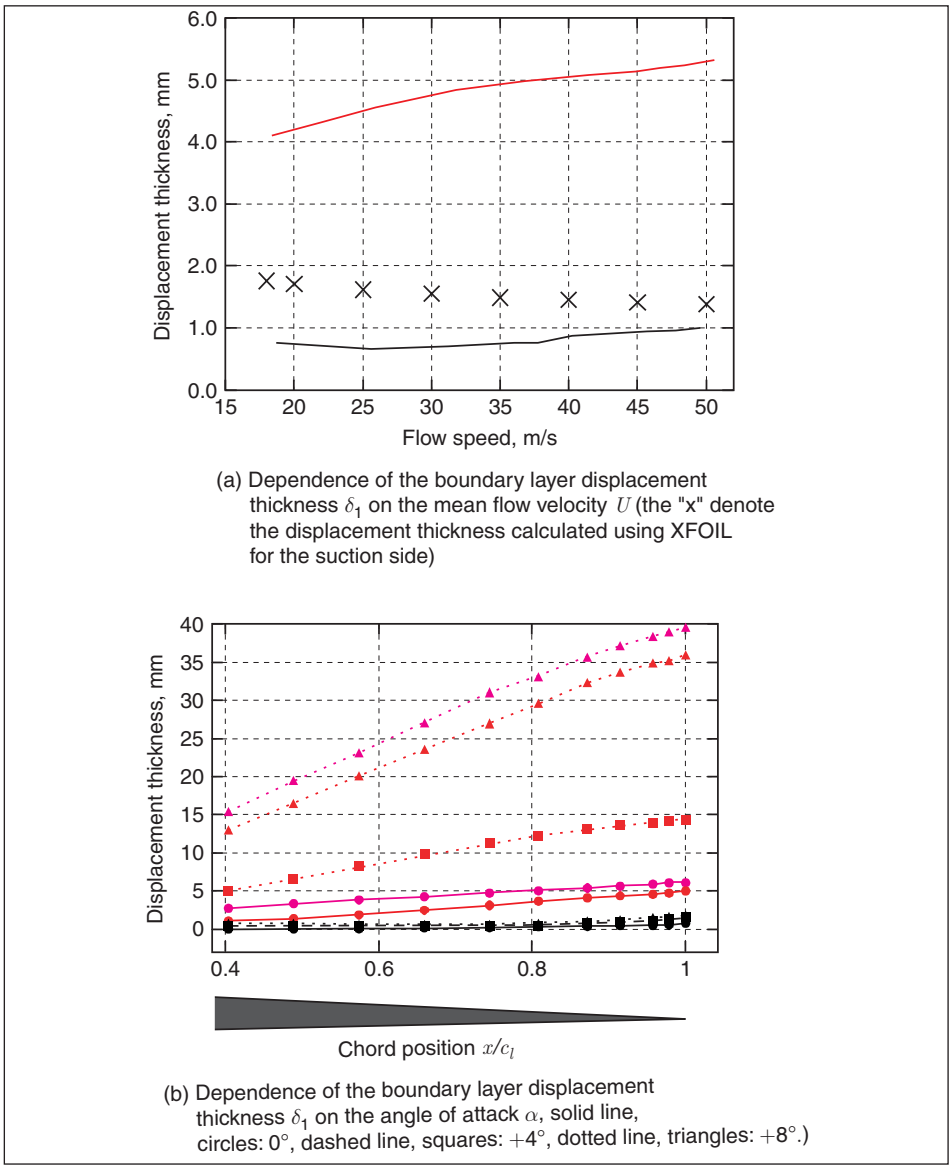

(a) Dependence of the boundary layer displacement thickness δ_1 on the mean flow velocity U (the "x" denote the displacement thickness calculated using XFOIL for the suction side)

(b) Dependence of the boundary layer displacement thickness δ_1 on the angle of attack α, solid line, circles: 0°, dashed line, squares: +4°, dotted line, triangles: +8°.)

Figure 22. Dependence of the (suction side) boundary layer displacement thickness on the mean flow velocity U and the angle of attack a (r = ∞, 8,200, 1,000 Pa s/m²). Note that the schematic of the airfoil is given for illustrative purpose of the chordwise position only, the distance given on the ordinate refers to the airfoil surface.

The results of the hot–wire measurements in relation to the acoustic results indicate that despite an increasing boundary layer displacement thickness of the porous airfoils their overall trailing edge noise emission decreases and is noticeably below that of the reference airfoil. The turbulent boundary layer thickness as well as the boundary layer displacement thickness of the porous airfoils clearly depend on the air flow resistivity of the materials: For the examined porous materials the boundary layer thickness and the displacement thickness increase for decreasing air flow resistivities. For non–porous airfoils on the other hand, the theory by Ffowcs Williams and Hall (Equation 2) gives the opposite relation between the characteristic turbulent correlation scale and the noise generated at the trailing edge: If the mean flow speed is kept constant, the far field mean square sound pressure is proportional to the characteristic tturbulence correlation scale. The

characteristic turbulence correlation scale is thereby assumed to be proportional to the boundary layer thickness or the displacement thickness and the mean turbulence velocity is assumed to be proportional to the mean flow speed. This assumption can clearly not be made for the porous airfoils. Due to this reason, established airfoil self noise prediction models that are based on the analysis of Ffowcs Williams and Hall with the above mentioned assumptions, like the BPM–model or the more simple model by Lowson, can not be used without general modifications for the estimation of trailing edge noise generated by porous airfoils. The results presented in this paper may serve as a basis to develop a model for the influence of the porous material parameters on the trailing edge noise generation.

5. CONCLUSIONS

The present paper describes the research on the trailing edge noise reduction and the boundary layer properties of porous airfoils. The main objective is the investigation of the influence of the air flow resistivity of the porous materials on both the generation of noise at the trailing edge and on the turbulent boundary layer displacement thickness of the airfoils. Therefore, aeroacoustic measurements using a 56-channel microphone array as well as constant temperature anemometry measurements with a boundary layer probe have been performed on a set of SD7003–shaped airfoils. Four airfoils were made of flow permeable materials with different air flow resistivities and one non–porous airfoil served as a reference.

Apart from few exceptions, the sound pressure level generated at the trailing edge of the porous airfoils was lower than that of the reference airfoil over a large range of medium frequencies. For very high frequencies, e.g. in the 20 kHz third octave band, the porous airfoils generally produced more noise than the non–porous airfoil. This might be due to the contribution of the surface roughness noise, which is usually noticeable at high frequencies. This means that a considerable sound reduction effect was measured for the trailing edge noise of the porous materials despite a presumed contribution of surface roughness noise. A classical scaling approach that scales the generated sound pressure level with the 4.6th power of the flow speed was tested on the airfoils. While it yields good results for the reference airfoil, it does not fit very well for the porous airfoils. It was found that the turbulent boundary layer thickness and the boundary layer displacement thickness of the porous airfoils clearly exceed those of the non–porous airfoil for both suction and pressure side. The general trend is that the displacement thickness of the porous airfoils increases for decreasing flow resistivities.

Contrary to the theory for non–porous airfoils, an increasing turbulent boundary layer thickness and boundary layer displacement thickness result in a decreasing noise generation at the trailing edge of porous airfoils.

ACKNOWLEDGMENTS

This research was sponsored by the *Deutsche Forschungsgemeinschaft* in the priority program 1207, “Strömungsbeeinflussung in der Natur und Technik”, under the grant number SA 1502/1-2.

REFERENCES

[1] R. C. Chanaud. Noise reduction in propeller fans using porous blades at free-flow conditions. *The Journal of the Acoustical Society of America*, 51:15 –18, 1971.

[2] R. C. Chanaud, N. Kong., and R. B. Sitterding. Experiments on porous blades as a means of

reducing fan noise. *The Journal of the Acoustical Society of America*, 59:564–575, 1976.

[3] G. Savu and O. Trifu. Porous airfoils in transonic flow. *AIAA Journal*, 22:989–991, 1984.

[4] R. E. Mineck and P. M. Hartwich. Effect of full-chord porosity on aerodynamic characteristics of the NACA 0012 airfoil. *NASA Technical Paper 3591*, 1996.

[5] A. F. Tinetti, J. F. Kelly, S. X. S. Bauer, and R. H. Thomas. On the use of surface porosity to reduce unsteady lift. *31st AIAA Fluid Dynamics Conference and Exhibit*, 2001.

[6] A. F. Tinetti, J. F. Kelly, R. H. Thomas, and S. X. S. Bauer. Reduction of wake-stator interaction noise using passive porosity. *40th AIAA Aerospace Sciences Meeting and Exhibit*, 2002.

[7] A. Garcia-Sagrado, T. Hynes, and H. Hodson. Experimental investigation into trailing edge noise sources. *12th AIAA/CEAS Aeroacoustics Conference*, 2006.

[8] T. Geyer, E. Sarradj, and C. Fritzsche. Measurement of the noise generation at the trailing edge of porous airfoils. *Experiments in Fluids*, 48 (2):291–308, 2010.

[9] E. Sarradj and T. Geyer. Noise generation by porous airfoils. *13th AIAA/CEAS Aeroacoustics Conference*, 28, 2007.

[10] M. Herr. A noise reduction study on flow-permeable trailing-edges. Technical report, Deutsches Zentrum für Luft- und Raumfahrt (DLR), Institute of Aerodynamics and Flow Technology, 2007.

[11] W. K. Blake. *Mechanics of Flow-Induced Sound and Vibration, Volume I: General Concepts and Elementary Sources*. Academic Press, Inc., 1986.

[12] M. J. Lighthill. On sound generated aerodynamically. *Proceedings of the Royal Society of London. Series A, Mathematical and Physical Sciences*, 211:564–587, 1952.

[13] J. E. Ffowcs Williams and L. H. Hall. Aerodynamic sound generation by turbulent flow in the vicinity of a scattering halfplane. *Journal of Fluid Mechanics*, 40:657–670, 1970.

[14] T. F. Brooks and M. A. Marcolini. Scaling of airfoil self-noise using measured flow parameters. *AIAA Journal*, 23:207–213, 1985.

[15] M. S. Howe. A review of the theory of trailing edge noise. *Journal of Sound and Vibration*, 61:437–465, 1978.

[16] M. S. Howe. The displacement–thickness theory of trailing edge noise. *Journal of Sound and Vibration*, 75:239–250, 1981.

[17] T. F. Brooks and T. H. Hodgson. Trailing edge noise prediction from measured surface pressures. *Journal of Sound and Vibration*, 78:69–117, 1981.

[18] T. F. Brooks, D. S. Pope, and M. A. Marcolini. Airfoil self-noise and prediction. *NASA Reference Publication 1218*, 1989.

[19] F. W. Grosveld. Prediction of broadband noise from horizontal axis wind turbines. *Journal of Propulsion*, 1:292–299, 1985.

[20] M. V. Lowson. Assessment and prediction of wind turbine noise. *Flow Solutions Report*, 92/19:1–59, 1992.

[21] M. V. Lowson. A new prediction model for wind turbine noise. In *Renewable Energy, 17–19 November 1993*, 1993.

[22] S. Oerlemans and P. Migliore. Aeroacoustic wind tunnel tests of wind turbine airfoils. *AIAA Journal*, 3042, 2004.

[23] S. Oerlemans. Wind tunnel aeroacoustic tests of six airfoils for use on small wind turbines. Technical report, National Renewable Energy Laboratory, 2004.

[24] P. Moriarty. *NAFNoise User Guide*. National Wind Technology Center, 2005.

[25] M. S. Howe. On the generation of sound by turbulent boundary layer flow over a rough

wall. *Proceedings of the Royal Society of London A*, 395: 247–263, 1984.

[26] M. S. Howe. Surface pressures and sound produced by turbulent flow over smooth and rough walls. *Journal of the Acoustical Society of America*, 90:1041–1047, 1991.

[27] Y. Liu, A. P. Dowling, and H.-C. Shin. Effects of surface roughness on airframe noise. *12th AIAA/CEAS Aeroacoustics Conference*, 2006.

[28] Y. Liu, A. P. Dowling, H.-C. Shin, and A. R. Quayle. Experimental study of surface roughness noise. *13th AIAA/CEAS Aeroacoustics Conference*, 2007.

[29] D. L. Grissom. *A Study of Sound generated by a Turbulent Wall Jet Flow over Rough Surfaces*. PhD thesis, Virginia Polytechnic Institue and State University, 2007.

[30] A. S. Hersh. Experimental investigation of surface roughness generated flow noise. *8th AIAA Aeroacoustics Conference Paper 83–0786*, 1983.

[31] A. L. Braslow and E. C. Knox. Simplified method for determination of critical height of distributed roughness particles for boundary-layer transition at Mach numbers from 0 to 5. Technical report, National Advisory Committee for Aeronautics, Langley Aeronautical Laboratory, 1958.

[32] J. B. Barlow, W. H. Rae, and A. Pope. *Low–Speed Wind Tunnel Testing, 3rd edition*. John Wiley & Sons, New York, 1999.

[33] J. A. Schetz. *Boundary Layer Analysis*. Prentice Hall, Eaglewood Cliffs, New Jersey, 1993.

[34] M. S. Selig, J. Donovan, and D. Fraser. *Airfoils at Low Speeds*. SoarTech Aero Publications, 1989.

[35] ISO9053. Acoustics – materials for acoustical applications – determination of airflow resistance. Technical report, International Organization for Standardization, 1993.

[36] A. E. Scheidegger. *The Physics of Flow through Porous Media, 3. Edition*. University of Toronto Press, 1974.

[37] E. Sarradj, C. Fritzsche, T. Geyer, and J. Giesler. Acoustic and aerodynamic design and characterization of a small-scale aeroacoustic wind tunnel. *Applied Acoustics*, 70:1073–1080, 2009.

[38] M. Knight and T. A. Harris. Experimental determination of jet boundary corrections for airfoil tests in four open wind tunnel jets of different shapes. Technical report, NACA, Report No. 361, 1930.

[39] T. F. Brooks, M. A. Marcolini, and D. S. Pope. Airfoil trailing edge flow measurements and comparison with theorie incorporating open wind tunnel corrections. In *AIAA-84-2266, AIAA/NASA 9th Aeroacoustics Conference*, 1984.

[40] M. Drela. Xfoil: An analysis and design system for low Reynolds number airfoils. In *Conference on Low Reynolds Number Aerodynamics, University of Notre Dame*, 1989.

[41] C. Schulze, E. Sarradj, and A. Zeibig. Characteristics of microphone arrays. In *Inter-Noise*, 2004.

[42] R. K. Amiet. Refraction of sound by a shear layer. *Journal of Sound and Vibration*, 58:467–482, 1978.

[43] A. Lauterbach, K. Ehrenfried, and L. Koop. Array measurements in wind tunnels with open test sections. *Berlin Beamforming Conference (BeBeC) 2008*, 2008.

[44] P. T. Soderman. *First chapter on Microphone Measurements in and out of Airstream in "Aeroacoustic Measurements"*. Springer Verlag, 2002.

[45] C. Tropea, A. L. Yarin, and J. F. Foss, editors. *Springer Handbook of Experimental Fluid Mechanics*. Springer Verlag Berlin Heidelberg, 2007.

[46] P. Bradshaw and G. P. Huang. The law of the wall in turbulent flow. *Proceedings of the Royal Society of London A*, 165–188, 1995.

[47] E. Sarradj. A fast signal subspace approach for the determination of absolute levels from phased microphone array measurements. *Journal of Sound and Vibration*, 329:1553–1569, 2010. (meanwhile published)

[48] T. F. Brooks and W. M. Humphreys. A deconvolution approach for the mapping of acoustic sources (DAMAS) determined from phased microphone arrays. *10th AIAA/CEAS Aeroacoustics Conference*, 2004.

[49] P. Sijtsma. Clean based on spatial source coherence. *13th AIAA/CEAS Aeroacoustics Conference*, 2007.

[50] H. H. Bruun. *Hot–Wire Anemometry*. Oxford Science Publications, New York, 1995.

[51] H. Schlichting and K. Gersten. *Boundary Layer Theory*. Springer-Verlag Berlin, 2000.

$2.3M FOR 1-2 DECIBELS LESS

The initial testing of noise control panels installed on the interstate 5 Ship Canal Bridge in Seattle shows they are not reducing traffic sounds as much as expected. Recent tests found a reduction of only a decibel or two. Officials had expected a reduction of four or five decibels. The Transportation Department had a contractor install 700 baffles under the highways upper deck at a cost of $2.3 million.

NOISE LIMITS FOR PICKETING STRIKERS

Can picketing strikers be stopped from making too much noise in a shopping mall? This is the issue that the High Court in Durban was called on to decide in the recent case of Growthpoint Properties Ltd v SACCAWU and others. In deciding the case the court had to find a balance between the rights of owners and occupiers to their property, to the environment and to trade, on the one hand, and the right of strikers to freedom of expression, to bargain collectively, to picket, protest and demonstrate peacefully on the other hand. The union members were picketing in the basement parking lot at La Lucia Shopping Mall in Durban in terms of a picketing agreement between SACCAWU and Dis-Chem (one of the tenants at the Mall which was owned by Growthpoint). Growthpoint sought an interdict against SACAAWU on the basis that the noise made by the picketers, amplified in the basement parking lot, was creating a nuisance. The noise levels had been measured by an expert as exceeding the legal limit set by regulation for noise-induced hearing loss. The court confirmed that all strikes and pickets have the potential to cause inconvenience and some nuisance to third parties not involved in the labour dispute. It also said it should be cautious to interfere with the exercise of the right to picket. It was satisfied it could hear the case because Growthpoint had based its case on the common law of nuisance and its constitutional rights to property, issues that fall under the High Court's jurisdiction. The court held that the right to picket was not unlimited and absolute. In this case tolerance levels were exceeded when Growthpoint and its tenants could not conduct business. The noise made by the picketers was persistent, intolerable and unacceptably high. Tenants and customers were prejudiced and businesses not party to the dispute lost revenue as customers went elsewhere. The noise also created an unhealthy environment. Growthpoint and its tenants were impeded from using their properties. Of importance was the court's view that SACCAWU and its members could have exercised their rights without so interfering with the business of Growthpoint and its tenants, by lowering their noise level. They were not precluded from demonstrating, picketing, carrying placards or from singing and chanting softly. The union was thus ordered to cease committing a nuisance at La Lucia Mall by shouting, chanting loudly, ululating or using any instrument or object which made a loud noise.